· Letter · Advances in Polar Science
doi: 10.13679/j.advps.2018.0036 June 2019 Vol. 30 No. 2: 149-164

# Early Cenozoic diorite and diabase from Doumer Island, Antarctic Peninsula: zircon U-Pb geochronology, petrogenesis and tectonic implications

CUI Jiawei*, HU Jianmin, PEI Junling, CHEN Hong, DU Xingxing & WEI Lijie

Institute of Geomechanics, Chinese Academy of Geological Sciences, Beijing 100081, China

**Received 26 August 2018; accepted 26 April 2019; published online 19 June 2019**

**Abstract** In order to understand the petrogenesis and tectonic setting of diorite and diabase units on Doumer Island, Antarctic Peninsula, this paper reports new laser ablation—inductively coupled plasma—mass spectrometry (LA-ICP-MS) zircon U-Pb, geochemical, and Lu-Hf isotopic data for the magmatism. The diorite and diabase samples yielded zircon U-Pb ages of 55.4 ± 0.3 and 52.8 ± 0.4 Ma, respectively. These samples are enriched in the large ion lithophile elements and the light rare earth elements, and are depleted in the high field strength elements. The zircons in these samples yield εHf (*t*) values from 9.03 to 11.87 and model ages (TDM2) of 342–524 Ma. The major, trace, rare earth element (REE), and Hf isotopic data for the diorites indicate that these units were formed by the mixing of magmas generated by (a) the partial melting of mantle wedge material that experienced fluid-metasomatism in a subduction zone setting, and (b) the melting of juvenile crustal material induced by the upwelling of mantle-derived magmas in a subduction–collision setting. The diabase units contain higher total REE concentrations than the diorite, indicating they were derived from a different source region. These samples also have higher $Mg^{\#}$ values and contain lower concentrations of Cr and Ni than the diorites, and have weakly negative Nb and Ta anomalies with Nb/Ta values of <3. The zircons in these samples yield εHf (*t*) values from 9.08 to 11.11 and model ages (TDM2) of 389–503 Ma. The major, trace, REE, and Hf isotopic compositions of the diabase units indicate that that they were derived from the mixing of depleted mantle-derived magmas with magmas generated by the melting of juvenile crustal material which was induced by the upwelling of the mantle into the crust. Overall the Cenozoic diorite and diabase on Doumer Island is related to subduction environment.

**Keywords** **intrusive, Zircon U-Pb dating, Lu-Hf isotope, subduction environment, Early Cenozoic, Doumer Island**

**Citation:** Cui J W, Hu J M, Pei J L, et al. Early Cenozoic diorite and diabase from Doumer Island, Antarctic Peninsula: zircon U-Pb geochronology, petrogenesis and tectonic implications. Adv Polar Sci, 2019, 30(2): 149-164, doi: 10.13679/j.advps.2018.0036

## 1 Introduction

The Antarctica can be divided into the East Antarctic Shield, the Southwestern Antarctic Orogenic Belt and the Transantarctic Mountains. The Antarctic Peninsula is located within the Southwestern Antarctic Orogenic Belt (Vaughan and Storey, 2000; Zheng et al., 2015). The geological and tectonic evolution of the Antarctic Peninsula is complex due to the tectonic activity of the Southern Pacific tectonic domain since the Mesozoic. The structural deformation and magmatism along its western margin which was caused by subduction of the paleo-Pacific plate beneath the western Antarctic Peninsula during the Cretaceous (Thomson et al., 1983; Storey and Garrett, 1985; Storey et al., 1996; Zheng et al., 2018) is particularly

* Corresponding author, E-mail:1cuijiawei1@163.com

complicated. The Cenozoic volcanic rocks of the Antarctic Peninsula with minor amounts of intrusive are concentrated on the South Shetland Islands and other islands that lie off the main peninsula (Ryan, 2007; Zheng et al., 2015; Zheng et al., 2018). As the product of subduction of the paleo-Pacific plate, these magmatic rocks recorded information about the tectonic evolution. The diorite from Doumer Island is related to the subduction environment (Zheng et al., 2018). The volcanic rocks on Nelson Island (66–56 Ma) and the Potter Peninsula (47.6±0.2 Ma) are related to the subduction of the Pacific Plate (Haase et al., 2012), whereas the 45–44 Ma andesites and granites on the Barton and Weaver peninsulas formed in a subduction tectonic setting (Wang et al., 2009). The volcanic rocks from Fildes Peninsula (52–56 Ma) also formed in a subduction setting (Gao et al., 2018). The 60–55 Ma diorite and granodiorite units on Booth and Gerlache straits are also related to the subduction of the Pacific Plate (Zheng et al., 2018). All of these data indicate that this region records significant early Paleogene magmatic activity associated with the subduction environment. The magmatic rocks are important for understanding subduction and crust growth processes. However previous studies of igneous rocks have mainly focused on pre-mid-Cretaceous rocks in the eastern Antarctic Peninsula and existing studies lack of Sr-Nd-Hf isotopic data, the Cenozoic igneous rocks in this area are relatively poorly studied (Birkenmajer, 1994, 1995; Pankhurst et al., 2000).

This paper presents the results of a systematic study of diorite and diabase units on Doumer Island, including new zircon LA-ICP-MS U-Pb, whole-rock major and trace element, and zircon Lu-Hf isotopic data. These data constrain the timing of the magmatism in this region and provide insights into the petrogenesis and tectonic setting of the igneous activity.

## 2 Geological setting and petrography

The Antarctic Peninsula can be divided into Eastern-, Central-, and Western domains by the eastern Palmer Land Shear Zone (Vaughan and Storey, 2000). The Eastern Domain is located to the east of the shear zone (Figure 1) and represents the former Gondwanan margin, preserving a magmatic and sedimentary record of subduction along the margin (Burton-Johnson and Riley, 2015). The Eastern Domain consists of Triassic turbidites, Jurassic alluvial fan deposits, extensive Jurassic silicic volcanism named Chon Aike Volcanic Group, and Neogene to recent alkaline volcanic rocks on James Ross Island. The Central Domain which remains poorly understood, lies to the west of the shear zone, is characterized by Mesozoic and older igneous and metaigneous units (Vaughan and Storey, 2000; Vaughan et al., 2012a, 2012b). The Western Domain includes Alexander and Adelaide islands as well as the South Shetland Islands (Vaughan and Storey, 2000). Alexander Island is separated from the Central Domain by the Late Cretaceous—early Paleogene George VI Sound rift and contains turbidites and Jurassic sedimentary units with minor amounts of Late Jurassic lava flows and sills, as well as Late Cretaceous to Eocene forearc volcanic rocks and plutons (McCarron and Millar, 1997). The South Shetland Islands are separated from the Central Domain by the Neogene Bransfield Strait rift and contain Cretaceous to Eocene volcanic rocks and plutons (Barker, 1982; Figure 1).

Doumer Island, close to Anvers Island within the Western Domain, is separated from the Central Domain by the Gerlache Strait rift (Vaughan and Storey, 2000). The island contains intrusions (Hooper, 1962) which are dominated by diorite units that are intruded by diabase dikes. The diorites are grey to dark grey in color, coarse-grained and massive, and contain euhedral to subhedral plagioclase (45%–55%), allotriomorphic to subhedral hornblende (10%–15%), allotriomorphic pyroxene (5%–10%), and subhedral alkali feldspar (20%–25%), along with accessory zircon and Ti, Fe and apatite (Figures 2a, 2b). The plagioclase is grey, 0.5–1.0 mm in size, and shows polysynthetic twinning; the hornblende is green, 0.3–0.5 mm in size, and is locally altered to chlorite; the pyroxene in these samples is green and is 0.3–0.5 mm in size, and the alkali feldspar is 0.7–1.0 mm in size and shows Carlsbad twinning.

One diabase dike in the study area strikes 132°–212°, is ~1.5 m wide, and is sub-vertical. It is grey-black in color, porphyritic, and contains 10%–15% phenocrysts of plagioclase, pyroxene (35%–45%), and hornblende (5%–10%). The sample experienced hydrothermal alteration (Figures 2c, 2d).

## 3 Analytical techniques

Five fresh diorite samples (FDH-7/1, FDH-7/2: FDH-7/4, FDH-7/5; FDH-7/8; Table 1) and three fresh diabase samples (FDH-7/7-1, FDH-7/7-2, FDH-7/7-3; Table 1) were selected for whole-rock major and trace element analyses at the National Research Center for Geoanalys, Beijing, China. Prior to analysis the samples were pulverized to 200 mesh. Major element concentrations were determined by X-ray fluorescence spectrometry (XRF) employing a PW4400 instrument, yielding duplicate relative standard deviations of <5%. Trace and rare earth element (REE) concentrations were determined by inductively coupled plasma—mass spectrometry (ICP-MS; PE300D). Prior to analysis, sample powders were digested in high-pressure Teflon bombs using a mixture of super-pure HF and $HNO_3$ for 2 d at ~100℃. This procedure involved evaporation to near dryness, refluxing with super-pure $HNO_3$, and drying twice until the powders were completely dissolved. Duplicate analyses of samples and rock standards yielded relative standard deviations of <5% for the majority of the trace elements. Major and trace element concentrations are given in Table 1.

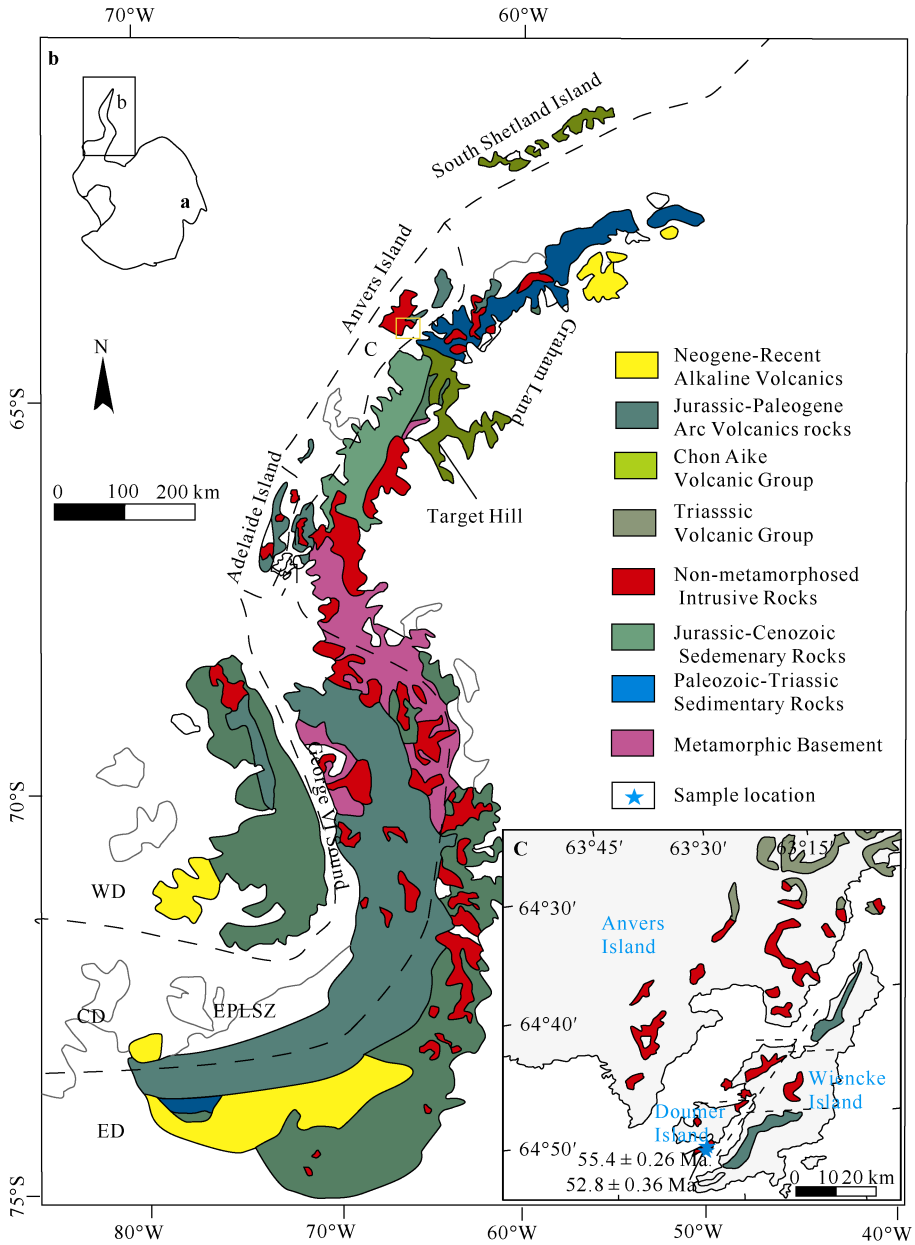


**Figure 1** Geological map of the Antarctic Peninsula (modified after Burton-Jonson et al., 2015). EPLSZ=East Palmer Land Shear Zone, WD=Western Domain, CD=Central Domain, ED=Eastern Domain. The locations of individual domains and the eastern Palmer Land Shear Zone are adapted from Vaughan and Storey (2000) and Vaughan et al. (2012a).

One sample from the diorite (FDH-7/3-1; Table.1) and one sample diabase (FDH-7/7-1; Table 1) were selected for zircon U-Pb analysis. Prior to analysis, the zircons were separated using standard heavy liquid techniques before individual grains were hand-picked under an optical microscope, avoiding those with visible impurities. The resulting zircon separates were mounted in epoxy resin before being imaged using reflected light and cathodoluminescence (CL) to identify internal structures and select sites for analysis. These zircons were analyzed by laser ablation (LA)-ICP-MS at the State Key Laboratory of Geological Processes and Mineral Resources, Wuhan, China, using the approached outlined by Liu et al. (2010). The resulting data were standardized using a 91500 standard zircon and a NIST610 glass standard, and were reduced using Isoplot v.3.0 (Ludwig, 2003), yielding weighted mean ages with $2\sigma$ uncertainties.

Zircon Hf isotopic compositions were determined by LA-multicollector (MC)-ICP-MS employing a Neptune Plus instrument combined with a Geolas 2005 excimer ArF laser ablation system at the State Key Laboratory of Geological Processes and Mineral Resources, Wuhan, China. These analyses used a 44 μm spot size, an 8 Hz

repetition rate, and a laser power of 60 m·(Jpulse)$^{-1}$. Operating conditions were the same as those described by Hu et al. (2015) and the resulting data were reduced using ICPMSDataCal (Liu et al., 2010).

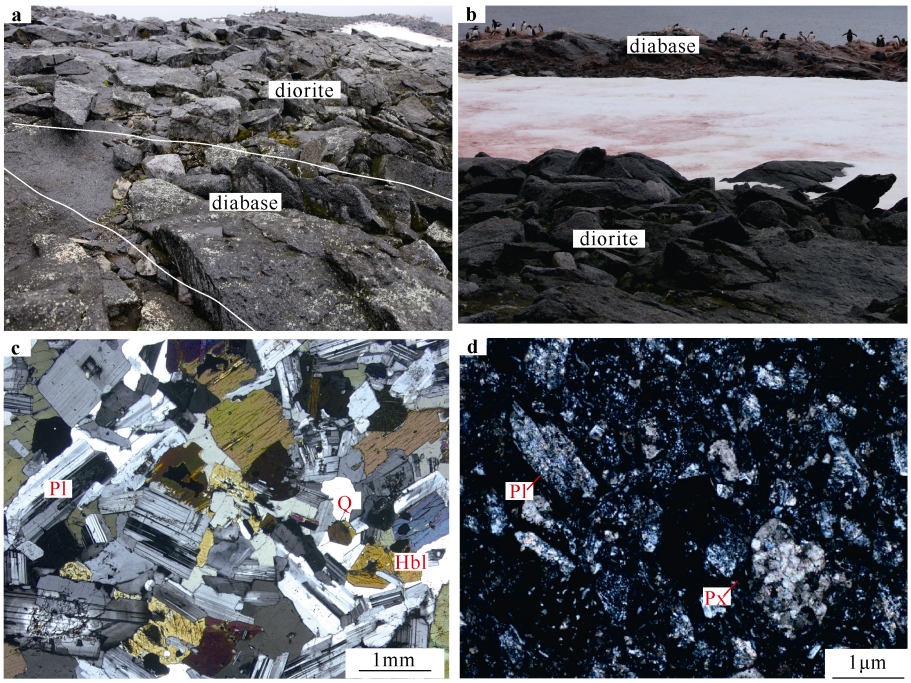


**Figure 2** Representative examples of the dolerite and diorite units on Doumer Island. Abbreviations are as follows and are after Whitney and Evans (2010): Q=quartz, Pl=plagioclase, Hbl= hornblende, Px=pyroxene.

**Table 1** Simplified sample descriptions and sampling location of plutonic rocks from Doumer Island

| | Sample | Lithology | Latitude | Longitude | Age |
|---|---|---|---|---|---|
| 1 | FDH-7/1 | diorite | 64°52′38″S | 63°34′41″W | / |
| 2 | FDH-7/2 | diorite | 64°52′38″S | 63°34′41″W | / |
| 3 | FDH-7/3 | diorite | 64°52′38″S | 63°34′41″W | 55.4 ± 0.3 Ma |
| 4 | FDH-7/4 | diorite | 64°52′31″S | 63°34′18″W | / |
| 5 | FDH-7/5 | diorite | 64°52′31″S | 63°34′18″W | / |
| 6 | FDH-7/7 | diabase | 64°52′33″S | 63°34′49″W | 52.8 ± 0.4 Ma |
| 7 | FDH-7/8 | diorite | 64°52′33″S | 63°34′49″W | / |

# 4 Results

## 4.1 Whole-rock geochemistry

The major and trace element compositions of the five fresh diorite and three fresh diabase samples are given in Table 2. The diorite samples contain low to moderate concentrations of $SiO_2$ (54.90–59.65 wt.%), high concentrations of $Na_2O$ (3.35–3.94 wt.%), and low concentrations of $K_2O$ (1.09–1.77 wt.%), yielding total alkali ($Na_2O+K_2O$) concentrations of 4.35–5.15 wt.%. These samples ploted on gabbrodiorites and diorites area in a total alkali vs. silica (TAS) diagram (Figure 3) and on calc-alkaline in a $SiO_2$ vs. $K_2O$ diagram (Figure 4), which is also supported by the Rittman index (1.31–1.59) and alkalic index (1.43–1.65) values. The diorites contain low to moderate concentrations of $Al_2O_3$ (13.93–14.82 wt.%), high concentrations of CaO (5.58– 7.59 wt.%). These samples also contain low concentrations of MgO (2.48–4.23 wt.%), have high total Fe expressed as FeO (TFeO) concentrations (7.23–9.00 wt.%), and have low $Mg^{\#}$ values (37.92–46.76; Willson, 1989).

The diabase samples contain low concentrations of $SiO_2$ (49.15–49.84 wt.%), high concentrations of $Na_2O$ (3.17–3.89 wt.%), and low concentrations of $K_2O$ (1.12–1.23 wt.%), yielding total alkali ($Na_2O+K_2O$) concentrations of 4.30–5.12 wt.%. These samples ploted on gabbros area in a TAS diagram (Figure 3) and on calc-alkaline area in a $SiO_2$ vs. $K_2O$ diagram (Figure 4), which is also supported by the Rittman index (1.42–1.56) and alkalic index (2.60–3.46) values. The samples contain high concentrations of MgO (8.52–8.82 wt.%) and TFeO (8.99–9.35 wt.%), and have moderate $Mg^{\#}$ values (62.46–62.82; Willson, 1989).

**Table 2** Major oxides composition (wt.%) and trace elements (ppm) of the diorite and diabase

| | Diabase | | | Diorite | | | | |
|---|---|---|---|---|---|---|---|---|
| | FDH-7/7-1 | FDH-7/7-2 | FDH-7/7-3 | FDH-7/1 | FDH-7/2 | FDH-7/4 | FDH-7/5 | FDH-7/8 |
| $SiO_2$ | 49.15 | 49.32 | 49.84 | 54.90 | 55.25 | 58.95 | 59.65 | 57.34 |
| $TiO_2$ | 1.49 | 1.54 | 1.53 | 0.78 | 0.87 | 0.87 | 0.90 | 0.77 |
| $Al_2O_3$ | 16.59 | 16.51 | 15.88 | 17.28 | 17.38 | 16.72 | 16.26 | 15.20 |
| $Fe_2O_3$ | 9.13 | 8.99 | 9.35 | 9.00 | 8.78 | 7.23 | 7.54 | 7.90 |
| MnO | 0.10 | 0.10 | 0.14 | 0.15 | 0.15 | 0.12 | 0.13 | 0.15 |
| MgO | 8.53 | 8.52 | 8.82 | 4.23 | 4.07 | 2.48 | 3.02 | 3.89 |
| CaO | 8.40 | 8.42 | 7.59 | 7.59 | 7.55 | 7.27 | 5.58 | 6.43 |
| $Na_2O$ | 3.18 | 3.17 | 3.89 | 3.35 | 3.46 | 3.84 | 3.94 | 3.55 |
| $K_2O$ | 1.12 | 1.23 | 1.23 | 1.09 | 1.11 | 1.77 | 1.45 | 1.71 |
| $P_2O_5$ | 0.27 | 0.29 | 0.29 | 0.26 | 0.27 | 0.22 | 0.23 | 0.18 |
| LOI | 1.88 | 1.78 | 1.59 | 0.76 | 0.53 | 1.40 | 1.04 | 1.61 |
| Total | 99.84 | 99.87 | 100.13 | 99.39 | 99.41 | 99.56 | 99.73 | 99.72 |
| La | 10.12 | 10.25 | 9.37 | 8.39 | 7.80 | 8.80 | 8.65 | 8.76 |
| Ce | 26.84 | 27.39 | 25.69 | 19.69 | 18.49 | 19.00 | 18.06 | 18.77 |
| Pr | 4.06 | 4.10 | 4.12 | 3.01 | 2.83 | 2.80 | 3.00 | 3.17 |
| Nd | 17.49 | 17.34 | 18.38 | 14.25 | 13.98 | 14.10 | 14.18 | 14.57 |
| Sm | 4.50 | 4.58 | 4.79 | 3.46 | 3.15 | 3.71 | 3.60 | 3.89 |
| Eu | 1.32 | 1.32 | 1.31 | 0.95 | 0.93 | 1.08 | 1.00 | 1.08 |
| Gd | 4.68 | 4.90 | 5.19 | 3.42 | 3.24 | 3.26 | 3.35 | 3.33 |
| Tb | 0.83 | 0.87 | 0.91 | 0.65 | 0.61 | 0.63 | 0.68 | 0.67 |
| Dy | 4.78 | 5.05 | 5.32 | 3.98 | 3.83 | 4.13 | 3.82 | 3.91 |
| Ho | 0.96 | 1.02 | 1.07 | 0.86 | 0.83 | 0.81 | 0.84 | 0.83 |
| Er | 2.46 | 2.59 | 2.74 | 2.32 | 2.24 | 2.21 | 2.21 | 2.21 |
| Tm | 0.36 | 0.38 | 0.40 | 0.33 | 0.32 | 0.33 | 0.31 | 0.36 |
| Yb | 2.06 | 2.19 | 2.35 | 2.05 | 1.96 | 2.32 | 2.40 | 2.38 |
| Lu | 0.34 | 0.34 | 0.35 | 0.33 | 0.31 | 0.32 | 0.30 | 0.29 |
| Y | 28.14 | 29.76 | 31.24 | 20.04 | 19.02 | 20.09 | 20.61 | 20.94 |
| ΣREE | 80.80 | 82.32 | 81.99 | 63.69 | 60.52 | 63.49 | 62.40 | 64.23 |
| LREE | 64.33 | 64.98 | 63.66 | 49.75 | 47.18 | 49.49 | 48.49 | 50.25 |
| HREE | 16.47 | 17.34 | 18.33 | 13.94 | 13.34 | 14.00 | 13.92 | 13.98 |
| LREE/HREE | 3.91 | 3.75 | 3.47 | 3.57 | 3.54 | 3.53 | 3.48 | 3.59 |
| $(La/Yb)_N$ | 3.32 | 3.16 | 2.69 | 2.77 | 2.68 | 2.56 | 2.44 | 2.48 |
| $\delta$Eu | 0.87 | 0.85 | 0.80 | 0.84 | 0.88 | 0.93 | 0.86 | 0.90 |
| $\delta$Ce | 0.98 | 0.99 | 0.97 | 0.92 | 0.92 | 0.89 | 0.83 | 0.83 |
| Rb | 58.14 | 65.04 | 58.96 | 29.70 | 31.22 | 52.09 | 37.43 | 45.53 |
| Ba | 253.31 | 257.54 | 243.40 | 229.68 | 239.60 | 384.50 | 348.63 | 315.42 |
| Th | 3.07 | 2.88 | 2.26 | 3.03 | 2.96 | 3.35 | 4.13 | 3.94 |
| U | 0.64 | 0.66 | 0.61 | 0.94 | 0.58 | 1.03 | 1.04 | 1.13 |
| Nb | 5.84 | 5.69 | 5.83 | 2.34 | 2.67 | 3.37 | 3.56 | 2.88 |
| Ta | 0.33 | 0.33 | 0.33 | 0.19 | 0.21 | 0.25 | 0.26 | 0.23 |
| Sr | 377.97 | 392.12 | 221.34 | 420.05 | 418.35 | 386.14 | 360.77 | 355.84 |
| Zr | 109.25 | 110.76 | 120.27 | 66.22 | 60.10 | 73.72 | 72.17 | 80.54 |
| Hf | 2.79 | 2.86 | 2.94 | 2.04 | 2.02 | 2.00 | 2.05 | 2.01 |
| Ni | 83.96 | 79.02 | 118.98 | 47.90 | 39.12 | 11.99 | 39.23 | 35.47 |
| Cr | 208.30 | 142.88 | 232.84 | 40.59 | 35.72 | 6.06 | 29.50 | 67.18 |
| La/Nb | 1.73 | 1.80 | 1.61 | 3.58 | 2.92 | 2.61 | 2.43 | 3.04 |

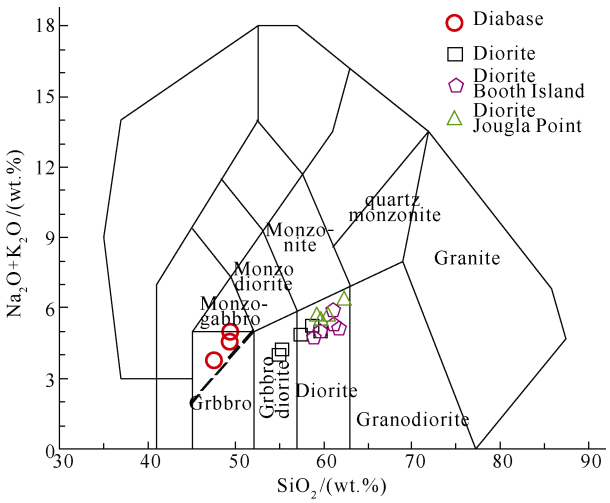


**Figure 3** Total alkali vs. silica (TAS) diagram (after Middlemost, 1994) for diorite and diabase samples from Doumer Island. The data of diorite from Booth Island and Jougla Island is cited from Zheng et al. (2018).

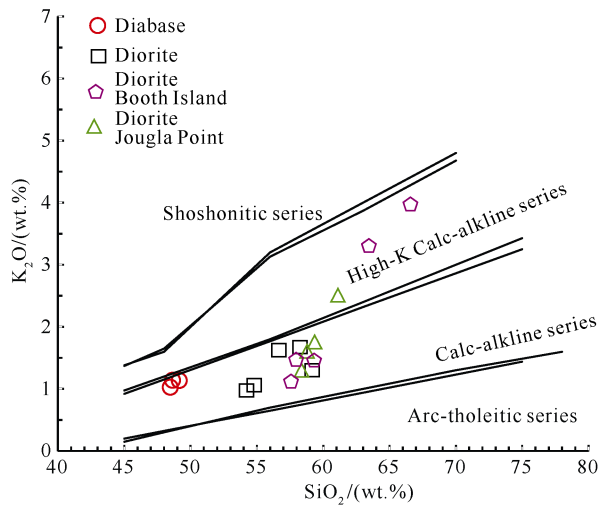


**Figure 4** $SiO_2$ vs. $K_2O$ diagram (after Peccerillo et al., 1976) for diorite and diabase samples from Doumer Island. The data of diorite from Booth Island and Jougla Island is cited from Zheng et al. (2018).

The diorites have low total REE (60.52–64.23 ppm), LREE (47.18–50.25 ppm), and HREE (13.34–14.00 ppm) concentrations that yield the ratio of LREE/HREE values of 3.48–3.59, and $(La/Yb)_N$ values of 2.44–2.77. The chondrite-normalized REE patterns is characteristic by LREE enriched, HREE depleted, and have weakly negative Eu anomalies (δEu=0.83–0.93; Figure 5a). The chondrite- normalized multi-element patterns is characteristic by enriched in the large ion lithophile elements (LILE; e.g., Rb, Ba, Th, U, and Sm) and depleted in the high field strength elements (HFSE; e.g., Nb, Ta, P, Zr, and Ti), indicating that these samples are similar to arc-type volcanic rocks (Willson, 1989; Figure 5b).

The diabase samples have higher total REE (80.80–82.32 ppm), LREE (63.66–64.98 ppm), and HREE (16.47–18.33 ppm) concentrations than the diorites, yielding LREE/HREE values of 3.53–3.59 and $(La/Yb)_N$ values of 3.47–3.91. The diabase samples have similar chondrite-normalized REE patterns that is characteristic by LREE-enriched, HREE-depleted, and weakly negative Eu anomalies (δEu = 0.80–0.87; Figure 5a). The N-MORB-normalized multi-element patterns are characteristic by selectively enriched in the LILE (e.g., Rb, Ba, Th, U, and Sm) and depleted in the HFSE (e.g., Nb, Ta, P, Zr, and Ti; Figure 5b).

## 4.2 Zircon U-Pb geochronology

Zircons from one fresh diorite sample and one fresh diabase sample were dated using LA-ICP-MS U-Pb analysis, with the results given in Table 3. The zircons within the diorite samples are off-white, long and prismatic, and euhedral or subhedral during CL imaging with lengths of 200–400 μm and length/width ratios of 1:1.2 to 1:3. The 25 analyzed zircons show oscillatory zoning during CL imaging and yield Th/U ratios of 0.438983–0.848528, both of which are indicative of a magmatic origin (Corfu et al., 2003). These analyses yielded a concordant $^{206}Pb/^{238}U$ age of 55.4 ± 0.3 Ma (*MSWD*=1.4) that is interpreted to represent the crystallization age of the diorite (Figure 6).

The zircons from the diabase are off-white, long and prismatic, euhedral or subhedral during CL imaging, with lengths of 50–80 μm and length/width ratios of 1:1.5 to 1:2. A total of 18 zircons from the diabase were analyzed, part of which show oscillatory zoning during CL imaging and others show less-developed diffusion zoning (e.g. FDH-7/7-07, FDH-7/7-15, FDH-7/7-18). All of them were eroded and yield Th/U ratios of 0.511361–0.819596, both of which are indicative of a magmatic origin (Corfu et al., 2003). These analyses yield a concordant $^{206}Pb/^{238}U$ age of 52.8±0.4 Ma (*MSWD*=1.2) that is interpreted to be the crystallization age of the diabase (Figure 7).

## 4.3 Zircon Lu-Hf isotopic geochemistry

The Lu-Hf isotopic compositions of 22 originally diorite-hosted zircons that yielded U-Pb ages from 54.0 to 56.8 Ma determined during this study (Table 4). These zircons yielded initial $^{176}Yb/^{177}Hf$ ratios of 0.011058–0.063900, $^{176}Lu/^{177}Hf$ ratios of 0.000374–0.001869, εHf(*t*) values of 9.03–11.87, and Hf TDM2 ages of 342–524 Ma. The Lu-Hf isotopic compositions of 17 originally diabase-hosted zircons that yielded U-Pb ages from 51.4to 53.9 Ma, yielding initial $^{176}Yb/^{177}Hf$ ratios of 0.011436–0.037732, $^{176}Lu/^{177}Hf$ ratios of 0.000471– 0.001548, εHf(*t*) values of 9.08–11.11, and Hf TDM2 ages of 389–520 Ma. The zircons from the diabase and diorite units yield $f_{Lu/Hf}$ values (−0.96 to −0.98) that are lower than those expected for mafic (−0.34; Amelin et al., 2000) and salic (−0.72; Vervoort et al., 1996) crustal material, indicating that the TDM2 ages of these samples reflect the timing of separation of the magmas that formed these units from a depleted region of the mantle.

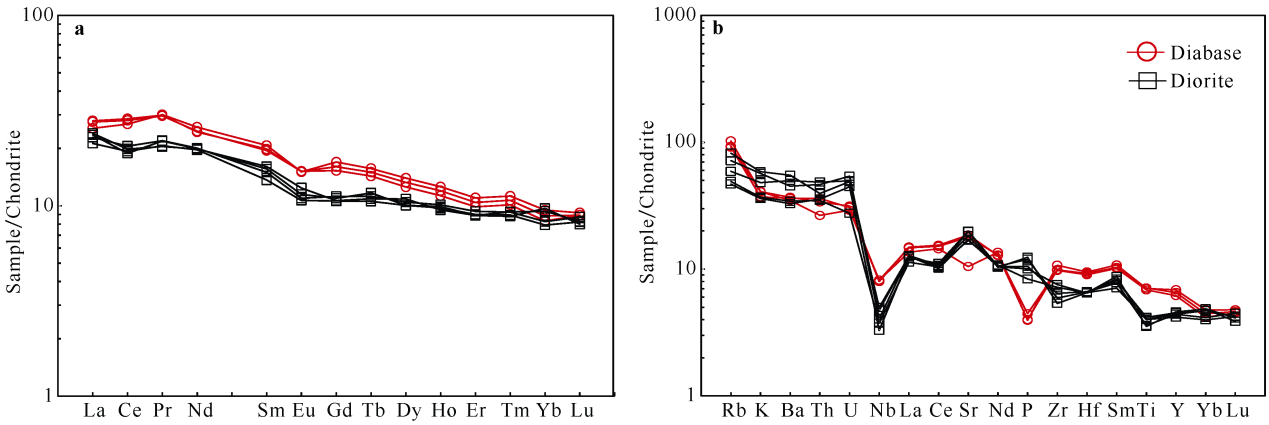


**Figure 5** Chondrite-normalized REE and multi-element patterns for diorite and diabase samples from Doumer Island normalized to the chondrite composition of Sun and McDonough (1989).

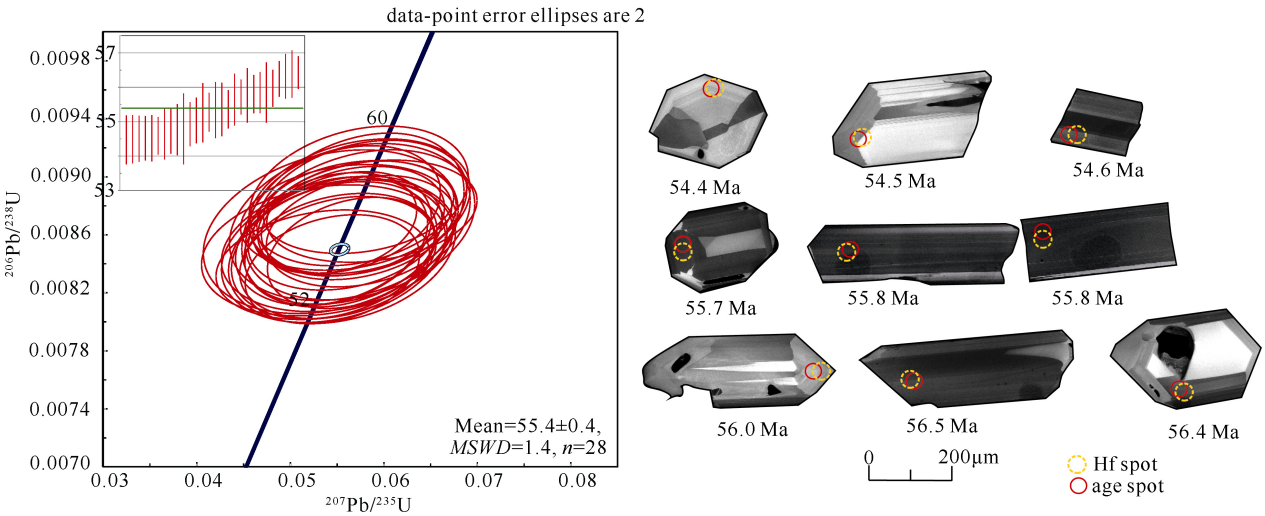


**Figure 6** U-Pb concordia diagram and associated CL images of zircons from the diorite sample from Doumer Island. Red circles and associated dates show the locations of individual LA-ICP-MS analyses.

# 5 Discussion

## 5.1 Petrogenesis

The diorite samples have a small range in $Mg^{\#}$ values (37.92–46.76) that are lower than the $Mg^{\#}$ values expected for primary magmas (~70; Willson, 1989), which suggests that these samples were derived from basaltic magmas that underwent fractionation or crustal contamination prior to emplacement. These samples are characterized by enrichment in the LILE and depletion in the HFSE (e.g., Nb, Ta, Ti, Zr, and Hf), suggesting that it may derived from the melt of recycle oceanic crust or mantle which experienced fluid-metasomatism and also suggest that the hornblende was the dominant mineral in the magma source (Zheng et al., 2018). The value ratio Rb/Sr （0.07–0.12）is close the value of upper matle (0.03) and far from the value of crust (0.4) (Taylor et al., 1995) which show that the diorite was derived from the mantle and experienced crustal contamination. Zircon is an extremely stable mineral that can survive erosion or metamorphism, contains high concentrations of Hf, and has low Lu/Hf ratios, making it ideal for the precise determination of initial Hf isotopic compositions. This in turn means that zircon Lu-Hf isotopic data can provide insights into the evolution of the Earth and the sourcing of magmas (Amelin et al., 1999). The Lu-Hf isotopic data of the diorite samples yield εHf($t$) values from 9.03 to 11.87, indicating that the diorite samples formed from a mantle-derived parental magma. The 342–524 Ma TDM2 ages for the diorite samples are similar to age of the basement material of the Antarctic Peninsula, indicating that the magmas generated by the partial melting of juvenile crustal material (Figure 8). Previous research has shown

**Table 3** U-Pb zircon LA-ICP-MS chronological data of samples

| | Total Pb | Th | U | Th/U | $^{207}Pb/^{206}Pb$ | | $^{207}Pb/^{235}U$ | | $^{206}Pb/^{238}U$ | | $^{207}Pb/^{206}Pb$ | | $^{207}Pb/^{235}U$ | | $^{206}Pb/^{238}U$ | | $^{208}Pb/^{232}Th$ | |
|---|---|---|---|---|---|---|---|---|---|---|---|---|---|---|---|---|---|---|
| | | | | | Ratio | 1 sigma | Ratio | 1 sigma | Ratio | 1 sigma | Age/Ma | 1 sigma | Age/Ma | 1 sigma | Age/Ma | 1 sigma | Age/Ma | 1 sigma |
| FDH-7/7-01 | 0.66 | 32.7 | 63.9 | 0.511361 | 0.0534 | 0.0081 | 0.0524 | 0.0067 | 0.0079 | 0.0002 | 346 | 307.37 | 51.8 | 6.42 | 50.5 | 1.38 | 50.8 | 3.20 |
| FDH-7/7-02 | 1.40 | 106 | 130 | 0.813197 | 0.0473 | 0.0055 | 0.0534 | 0.0056 | 0.0080 | 0.0002 | 64.9 | 255.52 | 52.8 | 5.39 | 51.4 | 1.14 | 55.5 | 2.32 |
| FDH-7/7-03 | 1.02 | 85.0 | 107 | 0.793375 | 0.0518 | 0.0061 | 0.0528 | 0.0051 | 0.0080 | 0.0002 | 276 | 248.12 | 52.3 | 4.97 | 51.7 | 1.32 | 42.0 | 2.64 |
| FDH-7/7-04 | 1.46 | 99.0 | 132 | 0.752519 | 0.0499 | 0.0053 | 0.0541 | 0.0053 | 0.0081 | 0.0002 | 191 | 229.6 | 53.5 | 5.15 | 52.3 | 1.19 | 54.8 | 2.46 |
| FDH-7/7-05 | 1.45 | 101 | 136 | 0.745126 | 0.0474 | 0.0047 | 0.0528 | 0.0047 | 0.0082 | 0.0002 | 77.9 | 222.19 | 52.3 | 4.57 | 52.4 | 1.11 | 53.1 | 2.35 |
| FDH-7/7-06 | 2.45 | 189 | 234 | 0.806546 | 0.0464 | 0.0035 | 0.0515 | 0.0038 | 0.0082 | 0.0001 | 20.5 | 174.055 | 51.0 | 3.62 | 52.5 | 0.83 | 54.8 | 1.89 |
| FDH-7/7-07 | 1.31 | 93.3 | 119 | 0.782012 | 0.0484 | 0.0048 | 0.0527 | 0.0043 | 0.0082 | 0.0002 | 117 | 227.745 | 52.1 | 4.13 | 52.5 | 1.18 | 54.1 | 2.31 |
| FDH-7/7-08 | 1.45 | 97.9 | 141 | 0.694006 | 0.0480 | 0.0046 | 0.0539 | 0.0048 | 0.0082 | 0.0002 | 98.2 | 211.08 | 53.3 | 4.58 | 52.7 | 1.09 | 57.7 | 2.57 |
| FDH-7/7-09 | 1.33 | 97.0 | 118 | 0.819596 | 0.0481 | 0.0048 | 0.0524 | 0.0045 | 0.0082 | 0.0002 | 102 | 222.19 | 51.9 | 4.29 | 52.7 | 1.17 | 59.8 | 2.70 |
| FDH-7/7-10 | 1.52 | 109 | 139 | 0.789063 | 0.0484 | 0.0044 | 0.0541 | 0.0042 | 0.0083 | 0.0002 | 120 | 199.97 | 53.5 | 4.02 | 53.1 | 1.07 | 54.3 | 2.24 |
| FDH-7/7-11 | 1.54 | 107 | 140 | 0.763497 | 0.0470 | 0.0048 | 0.0522 | 0.0049 | 0.0083 | 0.0002 | 55.7 | 216.635 | 51.7 | 4.71 | 53.1 | 1.06 | 54.0 | 2.39 |
| FDH-7/7-12 | 1.63 | 110 | 152 | 0.725103 | 0.0475 | 0.0043 | 0.0538 | 0.0043 | 0.0083 | 0.0002 | 76.0 | 199.97 | 53.2 | 4.13 | 53.2 | 1.10 | 56.5 | 2.44 |
| FDH-7/7-13 | 0.84 | 48.5 | 82.9 | 0.584731 | 0.0515 | 0.0060 | 0.0543 | 0.0049 | 0.0083 | 0.0002 | 265 | 257.38 | 53.7 | 4.70 | 53.3 | 1.36 | 36.1 | 2.86 |
| FDH-7/7-14 | 0.89 | 49.1 | 84.8 | 0.579407 | 0.0486 | 0.0056 | 0.0534 | 0.0057 | 0.0083 | 0.0002 | 132 | 257.37 | 52.8 | 5.50 | 53.4 | 1.39 | 49.9 | 2.89 |
| FDH-7/7-15 | 0.88 | 44.6 | 83.7 | 0.532892 | 0.0465 | 0.0052 | 0.0563 | 0.0056 | 0.0083 | 0.0002 | 33.4 | 238.855 | 55.6 | 5.39 | 53.5 | 1.44 | 53.5 | 3.05 |
| FDH-7/7-16 | 2.07 | 141 | 189 | 0.74433 | 0.0485 | 0.0037 | 0.0545 | 0.0038 | 0.0084 | 0.0002 | 124 | 174.05 | 53.9 | 3.67 | 53.7 | 0.98 | 55.4 | 1.98 |
| FDH-7/7-17 | 1.93 | 127 | 178 | 0.716713 | 0.0480 | 0.0047 | 0.0535 | 0.0047 | 0.0084 | 0.0002 | 98.2 | 224.04 | 52.9 | 4.50 | 53.9 | 0.99 | 59.8 | 2.37 |
| FDH-7/7-18 | 1.89 | 128 | 167 | 0.767138 | 0.0511 | 0.0044 | 0.0550 | 0.0042 | 0.0084 | 0.0005 | 256 | 196.2725 | 54.4 | 4.06 | 54.0 | 3.13 | 64.6 | 2.56 |
| FDH-7/3-01 | 1.67 | 109 | 148 | 0.734667 | 0.0480 | 0.0044 | 0.0551 | 0.0043 | 0.0084 | 0.0002 | 98.2 | 203.67 | 54.5 | 4.13 | 54.2 | 1.10 | 59.5 | 2.59 |
| FDH-7/3-02 | 2.52 | 194 | 224 | 0.866607 | 0.0502 | 0.0036 | 0.0565 | 0.0036 | 0.0085 | 0.0002 | 206 | 162.9425 | 55.8 | 3.50 | 54.4 | 1.00 | 55.2 | 1.82 |
| FDH-7/3-03 | 0.75 | 38.3 | 69.3 | 0.552219 | 0.0522 | 0.0071 | 0.0558 | 0.0065 | 0.0085 | 0.0003 | 295 | 281.455 | 55.1 | 6.22 | 54.4 | 1.72 | 58.0 | 4.71 |
| FDH-7/3-04 | 1.07 | 76.4 | 90.1 | 0.848582 | 0.0505 | 0.0063 | 0.0555 | 0.0050 | 0.0085 | 0.0002 | 217 | 266.635 | 54.9 | 4.77 | 54.5 | 1.30 | 55.6 | 2.48 |
| FDH-7/3-05 | 1.17 | 54.6 | 115 | 0.474795 | 0.0485 | 0.0050 | 0.0547 | 0.0049 | 0.0085 | 0.0002 | 120 | 229.595 | 54.1 | 4.75 | 54.5 | 1.29 | 52.7 | 2.94 |
| FDH-7/3-06 | 1.63 | 109 | 148 | 0.737241 | 0.0500 | 0.0043 | 0.0568 | 0.0044 | 0.0085 | 0.0002 | 198 | 185.155 | 56.1 | 4.19 | 54.5 | 1.22 | 51.7 | 2.82 |
| FDH-7/3-07 | 1.50 | 96.7 | 135 | 0.715635 | 0.0478 | 0.0053 | 0.0535 | 0.0053 | 0.0085 | 0.0002 | 87.1 | 244.41 | 53.0 | 5.14 | 54.5 | 1.18 | 57.0 | 2.72 |
| FDH-7/3-08 | 1.35 | 96.6 | 122 | 0.793168 | 0.0472 | 0.0044 | 0.0547 | 0.0045 | 0.0085 | 0.0002 | 61.2 | 272.185 | 54.1 | 4.32 | 54.5 | 1.24 | 56.4 | 2.46 |

Continued

| | Total Pb | Th | U | Th/U | $^{207}Pb/^{206}Pb$ | | $^{207}Pb/^{235}U$ | | $^{206}Pb/^{238}U$ | | $^{207}Pb/^{206}Pb$ | | $^{207}Pb/^{235}U$ | | $^{206}Pb/^{238}U$ | | $^{208}Pb/^{232}Th$ | |
|---|---|---|---|---|---|---|---|---|---|---|---|---|---|---|---|---|---|---|
| | | | | | Ratio | 1 sigma | Ratio | 1 sigma | Ratio | 1 sigma | Age/Ma | 1 sigma | Age/Ma | 1 sigma | Age/Ma | 1 sigma | Age/Ma | 1 sigma |
| FDH-7/3-09 | 2.65 | 141 | 268 | 0.527107 | 0.0484 | 0.0039 | 0.0553 | 0.0042 | 0.0085 | 0.0002 | 117 | 181.455 | 54.7 | 4.00 | 54.6 | 1.00 | 56.8 | 2.12 |
| FDH-7/3-10 | 1.20 | 90.7 | 110 | 0.82548 | 0.0508 | 0.0058 | 0.0559 | 0.0056 | 0.0085 | 0.0002 | 232 | 244.42 | 55.3 | 5.35 | 54.7 | 1.38 | 52.7 | 2.34 |
| FDH-7/3-11 | 0.96 | 48.5 | 92.5 | 0.524082 | 0.0483 | 0.0048 | 0.0575 | 0.0050 | 0.0087 | 0.0002 | 122 | 222.19 | 56.7 | 4.81 | 55.6 | 1.35 | 48.7 | 3.29 |
| FDH-7/3-12 | 2.20 | 149 | 196 | 0.759913 | 0.0472 | 0.0035 | 0.0548 | 0.0036 | 0.0087 | 0.0001 | 57.5 | 175.9 | 54.1 | 3.44 | 55.7 | 0.91 | 53.1 | 2.16 |
| FDH-7/3-13 | 0.94 | 47.8 | 92.4 | 0.516974 | 0.0463 | 0.0051 | 0.0564 | 0.0053 | 0.0087 | 0.0002 | 13.1 | 248.115 | 55.7 | 5.06 | 55.8 | 1.41 | 57.7 | 3.96 |
| FDH-7/3-14 | 2.47 | 177 | 224 | 0.78951 | 0.0467 | 0.0035 | 0.0567 | 0.0040 | 0.0087 | 0.0002 | 31.6 | 179.605 | 56.0 | 3.84 | 55.8 | 0.99 | 53.2 | 1.78 |
| FDH-7/3-15 | 1.82 | 133 | 160 | 0.830821 | 0.0484 | 0.0040 | 0.0571 | 0.0043 | 0.0087 | 0.0002 | 120 | 185.155 | 56.4 | 4.16 | 55.8 | 1.07 | 55.2 | 2.01 |
| FDH-7/3-16 | 1.05 | 71.1 | 96.1 | 0.739958 | 0.0518 | 0.0056 | 0.0567 | 0.0049 | 0.0087 | 0.0002 | 276 | 251.8225 | 56.0 | 4.67 | 55.9 | 1.57 | 52.6 | 2.55 |
| FDH-7/3-17 | 2.19 | 166 | 197 | 0.845128 | 0.0465 | 0.0039 | 0.0560 | 0.0046 | 0.0087 | 0.0001 | 33.4 | 183.31 | 55.3 | 4.43 | 56.0 | 0.95 | 55.0 | 2.24 |
| FDH-7/3-18 | 1.92 | 107 | 171 | 0.625226 | 0.0491 | 0.0042 | 0.0587 | 0.0046 | 0.0088 | 0.0001 | 154 | 188.86 | 58.0 | 4.40 | 56.2 | 0.92 | 62.8 | 4.48 |
| FDH-7/3-19 | 1.57 | 107 | 140 | 0.761925 | 0.0476 | 0.0038 | 0.0559 | 0.0042 | 0.0088 | 0.0002 | 79.7 | 181.455 | 55.2 | 4.01 | 56.3 | 1.15 | 55.3 | 2.67 |
| FDH-7/3-20 | 1.30 | 60.8 | 116 | 0.524542 | 0.0508 | 0.0048 | 0.0577 | 0.0046 | 0.0088 | 0.0002 | 235 | 19.4425 | 56.9 | 4.40 | 56.4 | 1.22 | 54.7 | 3.11 |
| FDH-7/3-21 | 2.54 | 105 | 239 | 0.438983 | 0.0471 | 0.0035 | 0.0573 | 0.0042 | 0.0088 | 0.0001 | 53.8 | 179.6 | 56.6 | 3.99 | 56.4 | 0.84 | 58.1 | 2.58 |
| FDH-7/3-22 | 1.90 | 116 | 167 | 0.691763 | 0.0482 | 0.0043 | 0.0574 | 0.0048 | 0.0088 | 0.0002 | 109 | 196.265 | 56.7 | 4.65 | 56.5 | 1.21 | 56.2 | 2.37 |
| FDH-7/3-23 | 0.99 | 66.5 | 87.1 | 0.763234 | 0.0510 | 0.0070 | 0.0561 | 0.0073 | 0.0088 | 0.0002 | 239 | 288.86 | 55.4 | 7.01 | 56.5 | 1.50 | 53.3 | 2.66 |
| FDH-7/3-24 | 1.57 | 111 | 142 | 0.781168 | 0.0497 | 0.0051 | 0.0573 | 0.0048 | 0.0089 | 0.0002 | 189 | 216.635 | 56.6 | 4.60 | 56.9 | 1.26 | 48.0 | 2.35 |
| FDH-7/3-25 | 2.17 | 122 | 204 | 0.59922 | 0.0466 | 0.0037 | 0.0589 | 0.0048 | 0.0091 | 0.0002 | 33.4 | 172.2 | 58.1 | 4.57 | 58.3 | 1.05 | 53.8 | 2.12 |

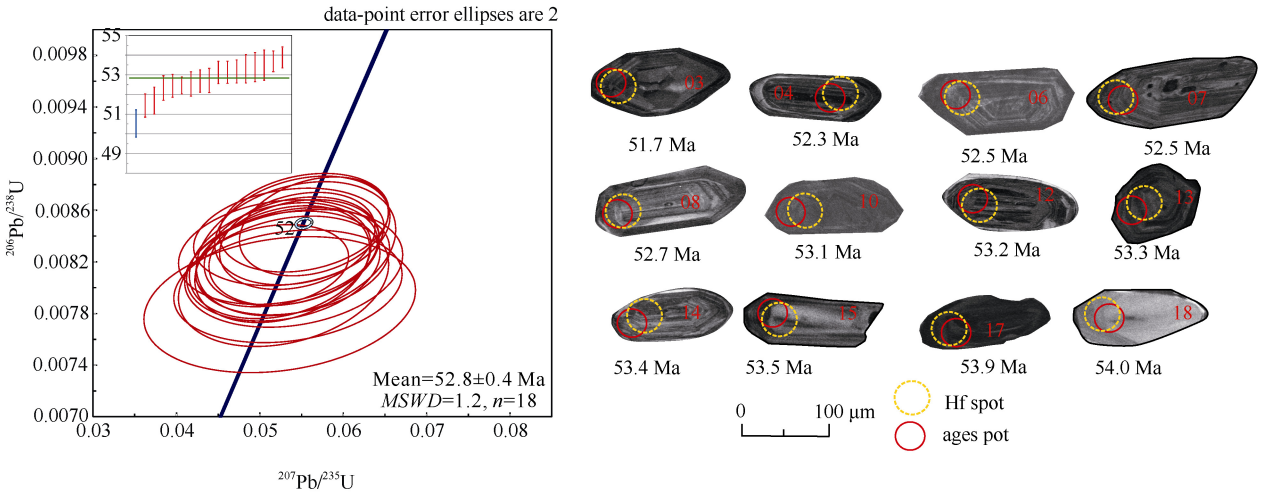


**Figure 7** U-Pb concordia diagram and associated CL images of zircons from the diabase sample from Doumer Island. Red circles and associated dates show the locations of individual LA-ICP-MS analyses.

that magmas derived from regions containing residual garnet have significantly fractionated HREE characteristics and Y/Yb ratios of >10, whereas magmas derived from regions containing residual hornblende have unfractionated HREE patterns and Y/Yb ratios close to 10 which indicated suggest that the source is characteristic with fluid rich. Above all the diorites was derived from mantle which experienced fluid-metasomatism (Sisson et al., 1994; Gao et al., 2003).

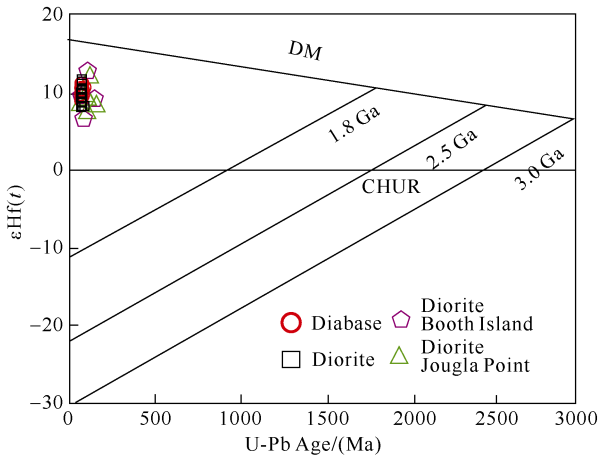


**Figure 8** Temporal variations in the Hf isotopic composition of diorite and diabase samples from Doumer Island. The data of diorite from Booth Island and Jougla Island is cited from Zheng et al. (2018).

The diorite is also characteristic by weakly negative Nb and Ta anomalies and La/Ta values (1.6–1.8) consistent with a subduction setting (Ernst et al., 1988; Rudnick et al., 2000). Harker diagrams for the diorite samples show negative correlations between CaO, MgO, TFeO, and $Al_2O_3$ with increasing $SiO_2$, and positive correlations between $K_2O$ and $Na_2O$ and increasing $SiO_2$ (Figure 9), indicating that the magam experienced the fractionation of pyroxene. In addition, the presence of negative correlations between $SiO_2$ and Cr and Ni indicates that the magam experienced record the crystallization of olivine.

The geochemical and Lu-Hf isotopic data indicate that the diorites formed as a result of the mixing of magmas derived from (a) the partial melting of mantle wedge material that experienced fluid-metasomatism in a subduction zone setting, and (b) the melting of juvenile crustal material induced by the upwelling of mantle-derived magmas.

The diabase samples contain higher total REE contents than the diorite samples, indicating that the former were derived from a different magma source. The diabase samples have a narrow range of $Mg^{\#}$ values (62.46–62.82) that are also lower than the values expected for primary magmas (~70; Wilson, 1989) which suggests that the diabase was derived from a basaltic magma that experienced fractionation and crustal contamination prior to emplacement. The diabase samples are depleted in Eu but are not depleted in Sr and Ba, suggesting that the magmas that formed these samples were derived from a source which experienced plagioclase fractionation. The diabase is also characteristic by weakly negative Nb and Ta anomalies and La/Ta values (1.6–1.8) consistent with a subduction setting (Ernst et al., 1988; Rudnick et al., 2000). The Cr and Ni concentrations of the diabase samples show negative correlations with $SiO_2$, suggesting that these samples record the crystallization of olivine (Figure 9). In addition, the diabase samples yield Hf($t$) values from 9.08 to 11.11, suggesting that these samples formed from magmas derived from a depleted region of the mantle; these diabase samples yield TDM2 ages (389–503 Ma) that are similar to the age of the basement material of the Antarctic Peninsula, indicating that the magma that formed the diabase was contaminated by the melting of juvenile crustal material (Figure 8). The geochemical and Lu-Hf isotopic data for the diabase samples indicate that they were derived from the

**Table 4** Zircon Hf isotopic compositions of the samples

| | $^{176}Hf/^{177}Hf$ | 1 se | $^{176}Lu/^{177}Hf$ | $^{176}Yb/^{177}Hf$ | $^{176}Hf/^{177}Hf(t)$ | $\varepsilon Hf(t)$ | 1 se | T(DM1) | T(DM2) | Hf Chur($t$) | Hf DM($t$) |
|---|---|---|---|---|---|---|---|---|---|---|---|
| FDH-7/7-1 | 0.283025 | 0.000015 | 0.001471 | 0.036705 | 0.283024 | 9.62 | 0.531662 | 326 | 485 | 0.282752 | 0.283213 |
| FDH-7/7-2 | 0.283016 | 0.000010 | 0.000487 | 0.011585 | 0.283016 | 9.33 | 0.359539 | 330 | 503 | 0.282752 | 0.283213 |
| FDH-7/7-3 | 0.283061 | 0.000011 | 0.000668 | 0.016312 | 0.283061 | 10.92 | 0.390169 | 268 | 401 | 0.282752 | 0.283213 |
| FDH-7/7-4 | 0.283067 | 0.000012 | 0.001262 | 0.032109 | 0.283066 | 11.11 | 0.405828 | 263 | 389 | 0.282752 | 0.283213 |
| FDH-7/7-5 | 0.283019 | 0.000009 | 0.000471 | 0.011436 | 0.283019 | 9.43 | 0.313726 | 326 | 497 | 0.282752 | 0.283213 |
| FDH-7/7-6 | 0.283056 | 0.000012 | 0.001453 | 0.037091 | 0.283055 | 10.73 | 0.417792 | 280 | 414 | 0.282752 | 0.283213 |
| FDH-7/7-7 | 0.283044 | 0.000011 | 0.001000 | 0.025282 | 0.283043 | 10.30 | 0.399408 | 295 | 441 | 0.282752 | 0.283213 |
| FDH-7/7-8 | 0.283037 | 0.000013 | 0.000647 | 0.015333 | 0.283036 | 10.07 | 0.470967 | 302 | 456 | 0.282752 | 0.283213 |
| FDH-7/7-9 | 0.283048 | 0.000011 | 0.001075 | 0.026945 | 0.283047 | 10.43 | 0.372559 | 290 | 433 | 0.282752 | 0.283213 |
| FDH-7/7-10 | 0.283009 | 0.000012 | 0.000616 | 0.014726 | 0.283009 | 9.08 | 0.42317 | 341 | 520 | 0.282752 | 0.283213 |
| FDH-7/7-11 | 0.283053 | 0.000010 | 0.000975 | 0.023845 | 0.283052 | 10.63 | 0.366316 | 281 | 420 | 0.282752 | 0.283213 |
| FDH-7/7-12 | 0.283051 | 0.000011 | 0.001548 | 0.037732 | 0.28305 | 10.53 | 0.398371 | 289 | 426 | 0.282752 | 0.283213 |
| FDH-7/7-13 | 0.283052 | 0.000010 | 0.001089 | 0.026647 | 0.283051 | 10.57 | 0.346168 | 284 | 424 | 0.282752 | 0.283213 |
| FDH-7/7-14 | 0.283062 | 0.000010 | 0.001378 | 0.033002 | 0.28306 | 10.91 | 0.351328 | 272 | 402 | 0.282752 | 0.283213 |
| FDH-7/7-15 | 0.283040 | 0.000008 | 0.001141 | 0.028284 | 0.283039 | 10.17 | 0.295226 | 301 | 450 | 0.282752 | 0.283213 |
| FDH-7/7-16 | 0.283052 | 0.000011 | 0.000920 | 0.022449 | 0.283051 | 10.63 | 0.382523 | 283 | 422 | 0.282751 | 0.283212 |
| FDH-7/7-17 | 0.283042 | 0.000012 | 0.001184 | 0.029144 | 0.28304 | 10.25 | 0.417006 | 300 | 446 | 0.282751 | 0.283212 |
| FDH-7/3-1 | 0.283043 | 0.000011 | 0.000890 | 0.021778 | 0.283042 | 10.29 | 0.377881 | 296 | 443 | 0.282751 | 0.283212 |
| FDH-7/3-2 | 0.283071 | 0.000012 | 0.001577 | 0.037310 | 0.28307 | 11.28 | 0.423935 | 260 | 380 | 0.282751 | 0.283212 |
| FDH-7/3-3 | 0.283049 | 0.000012 | 0.001647 | 0.038639 | 0.283047 | 10.50 | 0.431523 | 292 | 430 | 0.282751 | 0.283212 |
| FDH-7/3-4 | 0.283089 | 0.000011 | 0.002600 | 0.063900 | 0.283086 | 11.87 | 0.385844 | 241 | 342 | 0.282751 | 0.283212 |
| FDH-7/3-5 | 0.283068 | 0.000010 | 0.000802 | 0.019559 | 0.283068 | 11.21 | 0.350549 | 258 | 384 | 0.282751 | 0.283212 |
| FDH-7/3-6 | 0.283023 | 0.000011 | 0.000827 | 0.019236 | 0.283022 | 9.59 | 0.370697 | 323 | 488 | 0.282751 | 0.283212 |
| FDH-7/3-7 | 0.283074 | 0.000012 | 0.001869 | 0.044800 | 0.283072 | 11.37 | 0.404707 | 258 | 374 | 0.282751 | 0.283212 |
| FDH-7/3-8 | 0.283077 | 0.000010 | 0.001736 | 0.041740 | 0.283075 | 11.49 | 0.363963 | 252 | 366 | 0.282751 | 0.283212 |
| FDH-7/3-9 | 0.283047 | 0.000010 | 0.001496 | 0.036688 | 0.283046 | 10.45 | 0.336574 | 294 | 433 | 0.282751 | 0.283212 |

Continued

| | $^{176}Hf/^{177}Hf$ | 1 se | $^{176}Lu/^{177}Hf$ | $^{176}Yb/^{177}Hf$ | $^{176}Hf/^{177}Hf(t)$ | εHf($t$) | 1 se | T(DM1) | T(DM2) | Hf Chur($t$) | Hf DM($t$) |
|---|---|---|---|---|---|---|---|---|---|---|---|
| FDH-7/3-10 | 0.283072 | 0.000010 | 0.001441 | 0.034340 | 0.28307 | 11.31 | 0.344392 | 258 | 377 | 0.282751 | 0.283212 |
| FDH-7/3-11 | 0.283031 | 0.000010 | 0.000614 | 0.014545 | 0.283031 | 9.91 | 0.355189 | 309 | 468 | 0.282751 | 0.283212 |
| FDH-7/3-12 | 0.283039 | 0.000011 | 0.001093 | 0.026945 | 0.283038 | 10.17 | 0.391223 | 302 | 451 | 0.282751 | 0.283212 |
| FDH-7/3-13 | 0.283019 | 0.000010 | 0.000979 | 0.024500 | 0.283018 | 9.47 | 0.350996 | 330 | 496 | 0.282751 | 0.283212 |
| FDH-7/3-14 | 0.283008 | 0.000011 | 0.000537 | 0.012726 | 0.283008 | 9.10 | 0.400798 | 341 | 520 | 0.282751 | 0.283212 |
| FDH-7/3-15 | 0.283031 | 0.000009 | 0.000374 | 0.008299 | 0.28303 | 9.89 | 0.330528 | 308 | 469 | 0.282751 | 0.283212 |
| FDH-7/3-16 | 0.283041 | 0.000011 | 0.001676 | 0.041450 | 0.283039 | 10.20 | 0.402296 | 305 | 449 | 0.282751 | 0.283212 |
| FDH-7/3-17 | 0.283027 | 0.000012 | 0.000857 | 0.020691 | 0.283026 | 9.74 | 0.407607 | 318 | 479 | 0.282751 | 0.283212 |
| FDH-7/3-18 | 0.283030 | 0.000010 | 0.001387 | 0.033448 | 0.283029 | 9.83 | 0.332802 | 318 | 473 | 0.282751 | 0.283212 |
| FDH-7/3-19 | 0.283007 | 0.000011 | 0.001476 | 0.036060 | 0.283006 | 9.03 | 0.399257 | 351 | 524 | 0.282751 | 0.283212 |
| FDH-7/3-20 | 0.283027 | 0.000010 | 0.000482 | 0.011058 | 0.283026 | 9.76 | 0.366845 | 315 | 478 | 0.282751 | 0.283212 |
| FDH-7/3-21 | 0.283047 | 0.000012 | 0.001401 | 0.034040 | 0.283046 | 10.43 | 0.426624 | 293 | 434 | 0.282751 | 0.283212 |
| FDH-7/3-22 | 0.283052 | 0.000011 | 0.001136 | 0.028294 | 0.283051 | 10.62 | 0.390647 | 284 | 422 | 0.282751 | 0.283212 |

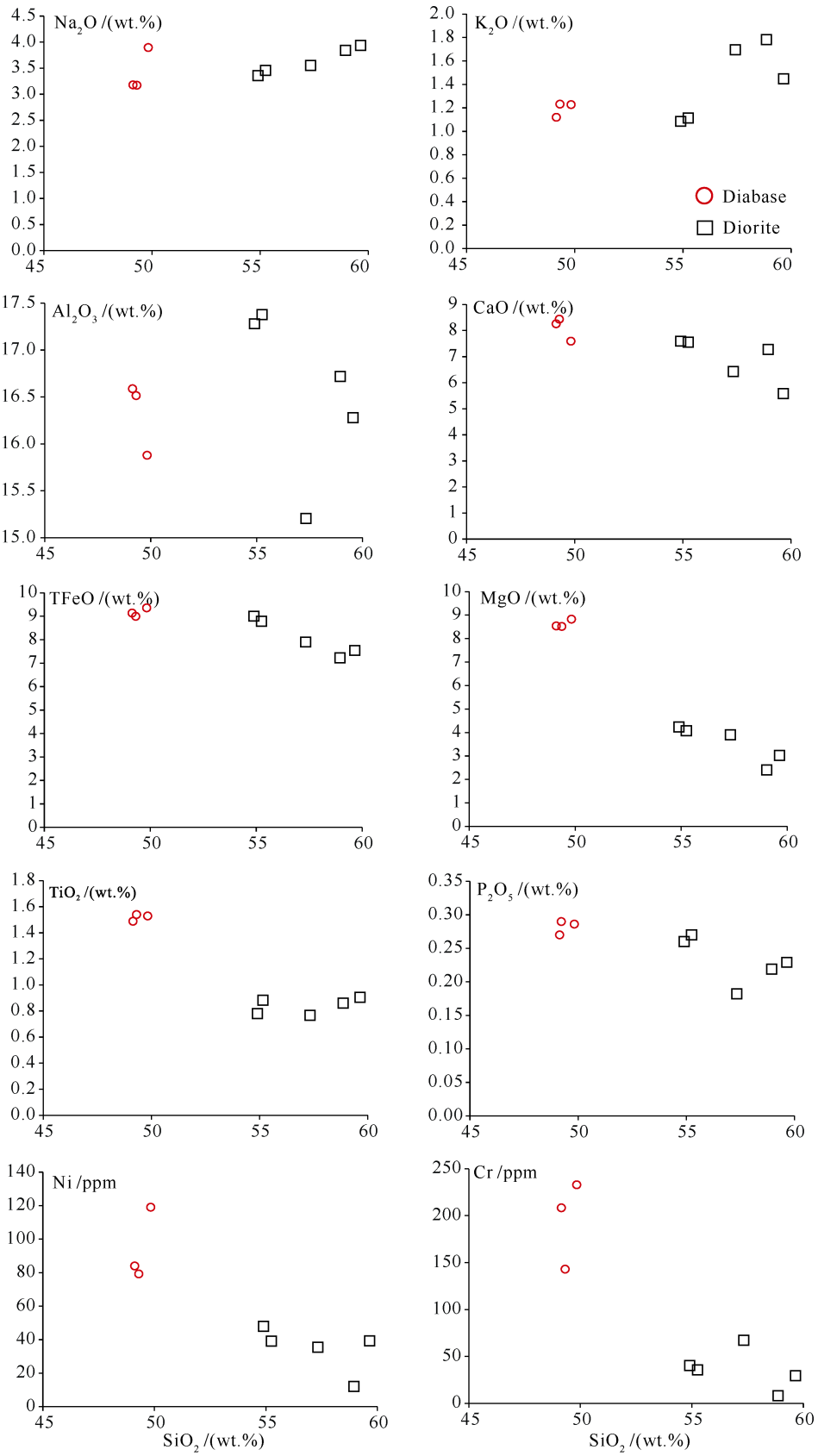


**Figure 9** Harker diagrams for diorite and diabase samples from Wiencke Island.

mixing of depleted mantle-derived magmas with magmas generated by the melting of juvenile crustal material which was induced by the upwelling of the mantle into the crust and did not experience significant crustal contamination but did crystallize pyroxene.

### 5.2 Tectonic evolution

Previous study show that the Antarctic Peninsula is a continental arc associated with the Gondwanan margin that developed during Mesozoic subduction beneath the supercontinent (Suarez, 1976) and was separated from Gondwana through extension of the Weddell Sea during Gondwana break-up (Jordan et al., 2017). The Early Cretaceous collision between the Central-Western and Eastern domains lasted until the mid-Cretaceous and was associated with the subduction of the Pacific Plate (Vaughan et al., 2012a, 2012b).

The zircon LA-ICP-MS dating of the diorite and diabase in the study area yielded magmatic ages of 55.4 ± 0.3 and 52.8 ± 0.4 Ma, respectively. The diorite and diabase samples ploted on the volcanic arc-related field in La/Nb vs La and Zr/Y vs Zr diagram (Figure 10; Li, 1993; Pearce et al., 1995). The diorite samples and diabase samples exhibit LILE enrichment and significant HFSE depletion, which is similar to subduction-related arc magmatic rocks (McCulloch and Gamble, 1991). This is also supported by their positive εHf(*t*) values, which suggest that these samples were derived from partial melting of juvenile crust with minor involvement of sediments or mantle materials in an arc setting. This is consistent with other studies of intrusive rocks from the Gerlache Strait area near Doumer Island which also suggest that the western Antarctic Peninsula was a subduction setting (Parada et al., 1990; Birkenmajer, 1995; Ryan, 2007; Zheng et al., 2018). The diorite and diabase in the study area is characteristics by positive εHf(*t*) values which is similar to arc-related diorite from Doumer Island (Zheng et al., 2018) . The samples were emplaced almost simultaneous with formation of the arc-related magmatism in the Gerlache Strait area (Zheng et al., 2018). The K-Ar and Rb-Sr isochron dating and zircon U-Pb dating show that the early Paleogene igneous rocks extensively developed along the western margin of the Antarctic Peninsula between 62–45 Ma (Ryan, 2007; Wang et al., 2009; Haase et al., 2012; Zheng et al., 2015; Gao et al., 2018; Zheng et al., 2018). The Antarctic Peninsula experienced a southward movement during 110–55 Ma and Southward translation during 55 to 27 Ma which formed the early Paleogene igneous rocks (Gao et al., 2018; Zheng et al., 2018).

Combining the new petrogenetic and geochronological data of this study with the results of previous research indicates that the Cenozoic diorite and diabase on Doumer Island is related to subduction environment (Birkenmajer, 1994; Ryan, 2007; Zheng et al., 2018).

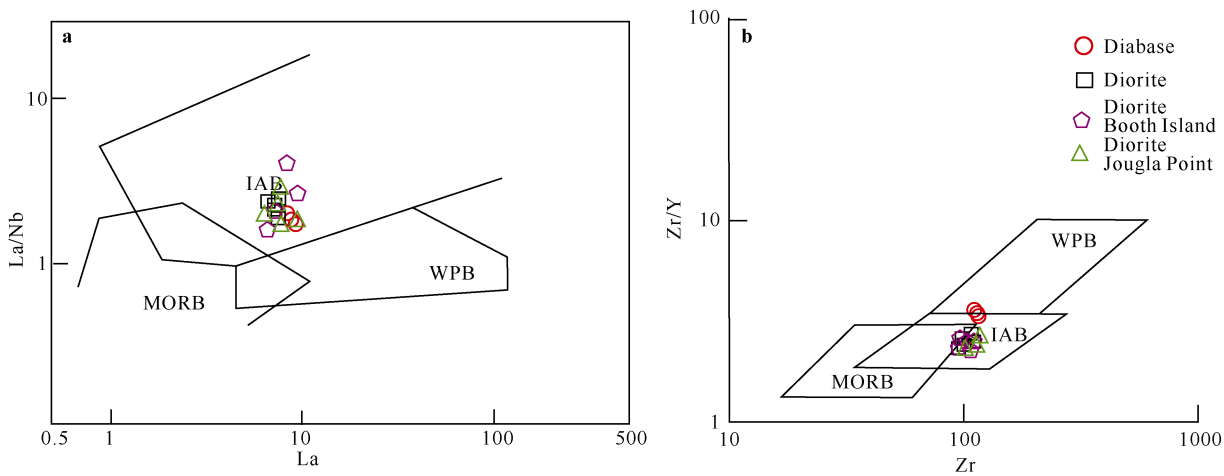


**Figure 10** Tectonic discrimination diagrams for diabase samples from Doumer Island. **a**, La/Nb vs La (Li, 1993); **b**, Zr/Y vs Zr diagram (Pearce et al., 1995). IAB—island-arc basalts; MORB—mid-ocean ridge basalts; WPB—within-plate basalts. The data of diorite from Booth Island and Jougla Island is cited from Zheng et al. (2018).

## 6 Conclusions

Based on analysis of the major, trace, rare earth element, and Hf isotopic data for the Early Cenozoic diorite and diabase from Doumer Island, Antarctic Peninsula, we conclude the following:

(1) Zircon LA-ICP-MS dating of diorite and diabase samples yielded magmatic ages of 55.4 ± 0.3 and 52.8 ± 0.4 Ma, respectively.

(2) The diorite formed by the mixing of (i) magmas generated by the partial melting of mantle wedge material that experienced fluid-metasomatism associated with subduction and slab breakoff, with (ii) magmas generated by the melting of juvenile crustal material induced by the upwelling of mantle-derived magmas. All of these occurred in a subduction tectonic setting. The diabase was derived from the mixing of depleted mantle-derived magmas with magmas generated by the melting of juvenile crustal

material. The geochemical and Lu-Hf isotopic data for the diabase samples indicate that they were derived from the mixing of depleted mantle-derived magmas with magmas generated by the melting of juvenile crustal material which was induced by the upwelling of the mantle into the crust and did not experience significant crustal contamination but did crystallize pyroxene;

(3) The Cenozoic diorite and diabase on Doumer Island is related to subduction environment.

**Acknowledgments** This research was financially supported by China Geological Survey (Grant no. DD20160060) and the National Natural Science Foundation of China (Grant nos. 4153209, 41872135). We thank Dr. Yong Yang and Dr. Xiaopeng Dong for their analytical assistance. We are also grateful to the Associate Editor Prof. Zhao Yue and the reviewer Philip Leaf for their constructive and detailed reviews and suggestions on the manuscript.

## References

Amelin Y, Lee D C, Halliday A N, et al. 1999. Nature of the earth's crust from hafnium isotopes in single detrital zircon. Nature, 399(6733): 252-255.

Barker P F. 1982. The Cenozoic subduction history of the Pacific margin of the Antarctic Peninsula: ridge crest–trench interactions. J Geol Soc London, 139(6): 787-801.

Birkenmajer K. 1994. Evolution of the Pacific margin of the northern Antarctic Peninsula: an overview. Geologische Rundshau, 83: 309-321.

Birkenmajer K. 1995. Geology of Gerlache Strait, West Antarctica. I. Arctowski Peninsula. Pol Polar Res, 16: 47-60

Burton-Johnson A, Riley T R. 2015. Autochthonous v. accreted terrane development of continental margins: a revised in situ tectonic history of the Antarctic Peninsula. J Geol Soc London, 172(6): 822-835.

Corfu F, Hanchar J M, Hoskin P W, et al. 2003. Atlas of zircon textures. Rev Mineral Geochem, 53(1), 469-500.

Ernst R E, Fowler A D, Pearce T H. 1988. Modelling of igneous fractionation and other processes using Pearce diagrams. Contrib Miner Petrol, 100(1): 12-18.

Gao L, Zhao Y, Yang Z, et al. 2018. New paleomagnetic and $^{40}Ar/^{39}Ar$ geochronological results for the South Shetland Islands, West Antarctica, and their tectonic implications. J Geophys Res: Solid Earth, 123(1): 4-30.

Gao Y F, Hou Z Q, Wei R H. 2003. Neogene porphyries from Gangdese: petrological, geochemical characteristics and geodynamic significances. Acta Petrol Sin, 19(3): 418-428 (in Chinese with English abstract).

Haase K M, Beier C, Fretzdorff S, et al. 2012. Magmatic evolution of the South Shetland Islands, Antarctica, and implications for continental crust formation. Contrib Miner Petrol, 163(6): 1103-1119.

Hooper P R. 1962. The petrology of Anvers Island and adjacent islands. Scientific Report, British Antarctic Survey, 47.

Hu, Z C, Zhang W, Liu Y S, et al. "Wave" signal smoothing and mercury removing device for laser ablation quadrupole and multiple collector ICP-MS analysis: application to lead isotope analysis. Anal Chem, 87: 1152-1157.

Jordan T A, Ferraccioli F, Leat P T. 2017. New geophysical compilations link crustal block motion to Jurassic extension and strike-slip faulting in the Weddell Sea Rift System of West Antarctica. Gondwana Res, 42: 29-48.

Leat P T, Flowerdew M J, Riley T R, et al. 2009. Zircon U-Pb dating of Mesozoic volcanic and tectonic events in north-west Palmer Land and south-west Graham Land, Antarctica. Antarct Sci, 21(6): 633-641.

Li S G. 1993. Ba-Nb-Th-La diagrams used to identify tectonic environments of ophiolite. Acta Petrol Sin, 9 (2): 146-157.

Liu Y S, Gao S, Hu Z C, et al. 2010. Continental and oceanic crust recycling-induced melt-peridotite interactions in the Trans-North China Orogen: U-Pb dating, Hf isotopes and trace elements in zircons of mantle xenoliths. J Petrol, 51: 537-571.

Ludwig K R. 2003. ISOPLOT 3.00: A geochronological toolkit for Microsoft Excel. Berkeley Geochronology Center, California, Berkeley, 39.

McCarron J J, Millar I L. 1997. The age and stratigraphy of fore-arc magmatism on Alexander Island, Antarctica. Geol Mag, 134(4): 507-522.

McCulloch M T, Gamble J A. 1991. Geochemical and geodynamical constraints on subduction zone magmatism. Earth Planet Sc Lett, 102(3-4): 358-374.

Middlemost E A. 1994. Naming materials in the magma/igneous rock system. Earth-Sci Rev, 37(3-4): 215-224.

Parada M A, Orsini J B, Ardil R, et al. 1990. The plutonic rocks of the southern Gerlache strait, Antarctica: geochronology, geochemistry and mineralogy. Symposium International "Geodynamique Andine": Grenoble, France, Conference Paper, 293-295.

Pankhurst R J, Riley T R, Fanning C M, et al. 2000. Episodic silicic volcanism in Patagonia and the Antarctic Peninsula: chronology of magmatism associated with the break-up of Gondwana. J Petrol, 41(5): 605-625.

Pearce J A, Baker P E, Harvey P K, et al. 1995. Geochemical evidence for subduction fluxes, mantle melting and fractional crystallization beneath the South Sandwich island arc. J Petrol, 36(4): 1073-1109.

Peccerillo A, Taylor S R. 1976. Geochemistry of Eocene calc-alkaline volcanic rocks from the Kastamonu area, northern Turkey. Contrib Miner Petrol, 58(1): 63-81.

Ryan C. 2007. Mesozoic to Cenozoic igneous rocks from Northwestern Graham Land: constraints on the tectonomagmatic evolution of the Antarctic Peninsula, Doctoral dissertation, University of Brighton.

Rudnick R L, Barth M, Horn I, et al. 2000. Rutile-bearing refractory eclogites: missing link between continents and depleted mantle. Science, 287(5451): 278-281.

Sisson T W. 1994. Hornblende-melt trace-element partitioning measured by ion microprobe. Chem Geol, 117(1-4): 331-344.

Storey B C, Garrett S W. 1985. Crustal growth of the Antarctic Peninsula by accretion, magmatism and extension. Geol Mag, 1985, 122(1): 5-14.

Storey B C, Vaughan A P M, Millar I L. 1996. Geodynamic evolution of the Antarctic Peninsula during Mesozoic times and its bearing on Weddell Sea history. J Geol Soc London, Special Publications, 108(1): 87-103.

Sun S S, McDonough W F. 1989. Chemical and isotopic systematics of oceanic basalts: Implications for mantle composition and processes// Saunders A D, Norry M J. Magmatism in the Ocean Basins. J Geol Soc London, Special Publication, 42(1): 313-345.

Suárez M. 1976. Plate-tectonic model for southern Antarctic Peninsula and its relation to southern Andes. Geology, 4(4): 211-214.

Thomson M R A, Pankhurst R J, Clarkson P D. 1983. The Antarctic

Peninsula a late Mesozoic-Cenozoic arc//Oliver R L, James P R, Jago J B. Antarctic Earth Science. Cambridge University Press, 323-327.

Vaughan A P M, Eagles G, Flowerdew M J. 2012a. Evidence for a two-phase Palmer Land event from crosscutting structural relationships and emplacement timing of the Lassiter Coast Intrusive Suite, Antarctic Peninsula: Implications for mid-Cretaceous Southern Ocean plate configuration. Tectonics, 31(1): TC1010, doi: 10.1029/2011 TC003006.

Vaughan A P, Leat P T, Dean A A, et al. 2012b. Crustal thickening along the West Antarctic Gondwana margin during mid-Cretaceous deformation of the Triassic intra-oceanic Dyer Arc. Lithos, 142: 130-147.

Vaughan A P, Storey B C. 2000. The eastern Palmer Land shear zone: a new terrane accretion model for the Mesozoic development of the Antarctic Peninsula. J Geol Soc London, 157(6): 1243-1256.

Vervoort J D, Pachelt P J, Gehrels G E, et al. 1996. Constraints on early Earth differentiation from hafnium and neodymium isotopes. Nature, 379(6566): 624-627.

Wang F, Zheng X S, Lee J I K, et al. 2009. An $^{40}Ar/^{39}Ar$ geochronology on a mid-Eocene igneous event on the Barton and Weaver peninsulas: Implications for the dynamic setting of the Antarctic Peninsula. Geochemistry, Geophysics, Geosystems, 2009, 10(12): Q12006, doi: 10.1029/2009GC002874.

Whalen J B, Currie K L, Chappell B W. 1987. A-type granites: geochemical characteristics, discrimination and petrogenesis. Contrib Miner Petrol, 95(4): 407-419.

Willson M. 1989. Igneous petrogenesis. A global tectonic approach. London, Boston, Sydney, Wellington: Unwin Hyman, 1-466.

Zheng G G, Liu X C, Zhao Y. 2015. Mesozoic-Cenozoic tectonomagmatic evolution of the Antarctic Peninsula and its correlation with Patagonia of Southernmost South America. Bull Miner Petrol Geochem, 34(6): 1090-1102 (in Chinese with English abstract).

Zheng G G, Liu X C, Zhao Y, et al. 2017. Mid-Cretaceous volcano-magmatism in the Curverville Island of the Antarctic Peninsula and its tectonic significance: constraints from zircon U-Pb geochronology and Hf isotopic compositions. Acta Petrol Sin, 33: 978-992 (in Chinese with English abstract).

Zheng G G, Liu X, Liu S, et al. 2018. Late Mesozoic—early Cenozoic intermediate—acid intrusive rocks from the Gerlache Strait area, Antarctic Peninsula: Zircon U-Pb geochronology, petrogenesis and tectonic implications. Lithos, 312: 204-222.